

DuCos: Duality Constrained Depth Super-Resolution via Foundation Model

Zhiqiang Yan¹ Zhengxue Wang² Haoye Dong¹ Jun Li² Jian Yang² Gim Hee Lee¹

¹National University of Singapore ²Nanjing University of Science and Technology

{yanzq, gimhee.lee}@nus.edu.sg

Abstract

We introduce *DuCos*, a novel depth super-resolution framework grounded in Lagrangian duality theory, offering a flexible integration of multiple constraints and reconstruction objectives to enhance accuracy and robustness. Our *DuCos* is the first to significantly improve generalization across diverse scenarios with foundation models as prompts. The prompt design consists of two key components: Correlative Fusion (CF) and Gradient Regulation (GR). CF facilitates precise geometric alignment and effective fusion between prompt and depth features, while GR refines depth predictions by enforcing consistency with sharp-edged depth maps derived from foundation models. Crucially, these prompts are seamlessly embedded into the Lagrangian constraint term, forming a synergistic and principled framework. Extensive experiments demonstrate that *DuCos* outperforms existing state-of-the-art methods, achieving superior accuracy, robustness, and generalization. The source codes and pre-trained models will be publicly available.

1. Introduction

Depth super-resolution (DSR) [56] is a fundamental task in computer vision that aims to restore high-resolution (HR) depth data from low-resolution (LR) depth inputs. It plays a crucial role in a wide range of downstream applications such as 3D reconstruction [4, 6, 44], augmented reality [35, 39, 51], and robotic sensing [24, 36, 46, 53]. These applications are largely reliant on clear and HR depth predictions. However, depth data typically has much lower resolution than color images¹ due to the differing advancements of color cameras and depth sensors. It is therefore essential to enhance the resolution of low-quality depth data.

Numerous advanced approaches have been developed, often using a reconstruction loss to minimize the discrepancy between depth predictions and ground truth annotations. However, this loss focuses predominantly on global

¹For example, the RGB-D system of the Huawei P30 Pro [6, 45] captures 3648×2736 color images while the depth maps are only 240×180 .

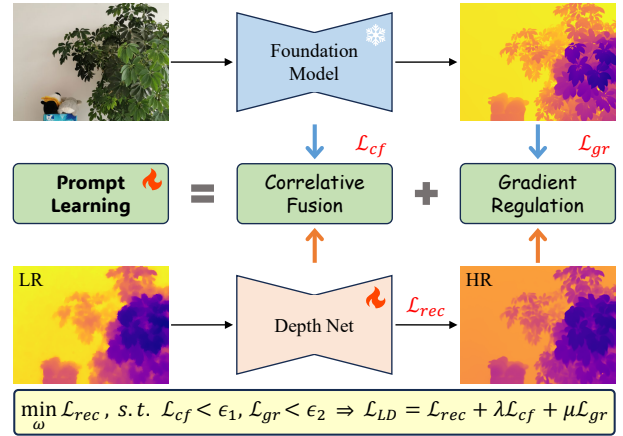


Figure 1. Overview of our **DuCos**: A highly synergistic system that integrates prompt learning with a Lagrangian duality (LD) based optimization algorithm. It combines the reconstruction loss with geometric consistency and edge preservation constraints to capture both global content and fine-grained local details, and uses foundation models to enhance generalization.

error minimization that relies heavily on pixel-level differences [36, 41, 53]. As a result, it often fails to capture fine-grained local geometric details, leading to blurred or over-smoothed depth recovery [13, 26, 44]. Moreover, the predictions become increasingly inaccurate and unreliable with disturbances such as noise in the input data. In addition, existing DSR solutions often focus on specialized network designs tailored to specific training data distributions. Despite their effectiveness in certain scenarios, these methods may face challenges in generalization across diverse resolutions and conditions.

We propose **DuCos**, a novel paradigm of **duality constrained DSR** via foundation model to address the above-mentioned issues. As illustrated in Fig. 1, *DuCos* establishes a theoretical framework for accurate and robust DSR while integrating prompt learning to enhance generalization. Specifically, our *DuCos* first reformulates DSR as a constrained optimization problem with the Lagrangian duality (LD) theory [1, 25]. The total LD loss comprises a reconstruction term and a constraint term. The reconstruction term minimizes global errors, while the constraint

term enforces geometric consistency and edge preservation. Guided by theoretical principles, this design allows the model to balance global context and local details, enhancing both accuracy and robustness. Furthermore, our DuCos is a pioneer in leveraging depth foundation models [8, 29, 47] as prompts to boost generalization. Concretely, these prompts consist of correlation fusion (CF) and gradient regulation (GR). CF quantifies the similarity between RGB-D features using the Pearson Correlation Coefficient and subsequently conducts recurrent fusion. Such explicit data statistics facilitate intuitive and effective modeling. In addition, while depth predictions from depth foundation models often exhibit significant errors, they retain remarkably sharp edges. To take advantage of this property, GR computes their gradients to highlight edges and subsequently minimizes the normalized gradient errors, leading to improved accuracy.

We further introduce an alignment loss in CF to enhance the geometric consistency between RGB-D features, and an edge-aware loss is designed in GR to promote edge preservation. These two loss functions are seamlessly integrated into the Lagrangian duality framework as the Lagrangian constraint term, resulting in a highly synergistic system capable of effectively capturing the sparsity and structural characteristics of depth maps.

In summary, our contributions are as follows:

- We present a novel DSR paradigm based on Lagrangian duality theory, reformulating it as a constrained optimization problem to ensure a precise solution with rigorous theoretical foundations.
- To our best knowledge, we are first to leverage foundation models as DSR prompts and seamlessly integrate them into the Lagrangian duality framework through CF and GR along with their respective constraints.
- Extensive experiments demonstrate the superiority of our approach over state-of-the-art methods in terms of accuracy, robustness, and generalization on five datasets.

2. Related Work

Depth Super-Resolution. Existing methods can be broadly categorized into synthetic DSR and real-world DSR, depending on the nature of the data used. For synthetic DSR, the degradation pattern is well defined [2, 3, 11, 24, 26, 37, 42, 53] since LR depth inputs are typically generated from depth annotations using bicubic interpolation. For example, ATGVNet [30] combines convolutional neural networks with total variation to produce HR depth maps. MS-GNet [9] introduces a multi-scale guidance network to enhance depth boundaries. PMBANet [49] presents a progressive multi-branch fusion network aimed at restoring high-resolution depth while maintaining sharp boundaries. Similarly, SSDNet [53, 54] incorporates discrete cosine transform and spherical contrast refinement to address issues related to fine details. Recently, several guided image filter-

ing approaches [13, 17, 41, 56] have been proposed to improve the transfer of guidance information into target depth maps. For example, DKN [13] utilizes deformable kernel networks to model sparse and spatially variant filter kernels, thereby improving the flexibility of filtering. Furthermore, advanced transformer [54] and diffusion [24] techniques are also incorporated to further advance the DSR task. With the increasing technical and practical demands, real-world DSR with unknown degradation patterns emerges. For the first time, FDSR [6] builds a real-world benchmark dataset and a new blind DSR baseline. Subsequently, SFGNet [51] introduces a structure flow-guided model that learns cross-modal flows to effectively propagate the structural information of color images. Most recently, DORNet [40] utilizes self-supervised degradation learning for the first time to model the degradation patterns of real-world data, contributing to significant performance improvements. Unlike these methods that are optimized using a fixed reconstruction loss function, our objective is to develop a highly precise and robust model with stronger theoretical guarantees.

Depth Prompt Learning. A variety of depth estimation foundation models [8, 12, 29, 47, 48, 50] from a single image have been proposed. These models can provide strong priors for various depth perception tasks, including depth matching [10, 43] and depth completion [19, 21, 23, 27, 28, 38]. DEFOM-Stereo integrates Depth Anything v2 [48] into RAFT-Stereo [20] to enhance stereo matching capabilities. FoundationStereo [43] enables robust and accurate zero-shot stereo depth estimation, bridging the gap between simulation and reality. To complete sparse depth maps, DepthPrompting [28] and UniDC [27] design a prompt mechanism that aggregates RGB priors from depth foundation models with depth features from depth-private branches. Marigold-DC [38] injects sparse depth observations as test-time guidance into a pretrained latent diffusion model for monocular depth estimation [12]. Furthermore, DepthLab [21] introduces image-conditioned depth inpainting based on diffusion priors, thereby facilitating various downstream applications. DepthRescaling [23] proposes to rescale Depth Anything predictions using 3D points provided by low-cost depth sensors or techniques. What’s more, PromptDA [19] achieves 4K resolution depth estimation from low-quality depth data through concise prompt fusion and scaling designs. All of these depth prompt learning methods provide valuable insights into harnessing the powerful prior knowledge of depth foundation models to benefit image-guided depth perception tasks.

3. Our Method: DuCos

Overview. Existing DSR methods focus mainly on specialized network designs. In contrast, our approach seeks to establish a general baseline by harnessing the strong pri-

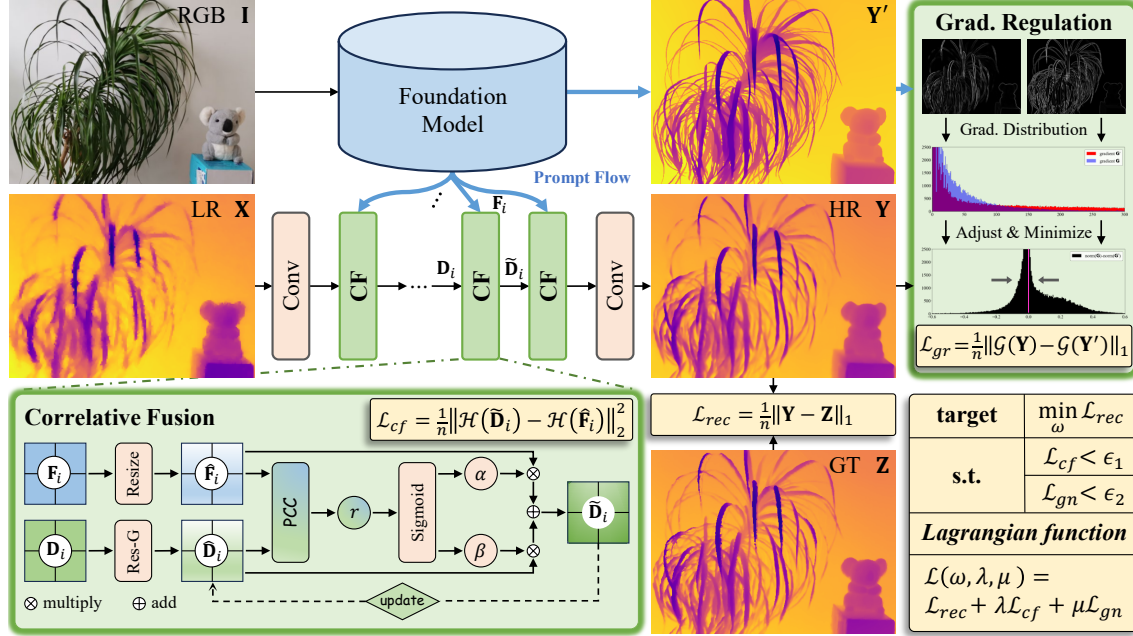


Figure 2. Detailed pipeline of DuCos. The color image I is first processed by a depth foundation model to generate prompt flows, including the intermediate features F_i and sharp-edged relative depth output Y' . F_i is then used to guide depth recovery with Correlative Fusion (CF), and Y' enhances edges through Gradient Regulation (GR). Moreover, CF and GR are both formulated as constraints on reconstruction loss within the Lagrangian duality framework. Res-G: residual group [52], PCC: Pearson Correlation Coefficient.

ors of depth foundation models, guided by theoretical principles. Fig. 2 shows the pipeline of our DuCos with two key components: prompt learning and Lagrangian duality optimization. For prompt learning, the prompt flow F_i and Y' is derived from a depth foundation model given a color image I . To effectively integrate these prompts, we first design correlative fusion (CF), which iteratively fuses the RGB prompt feature F_i and the depth feature D_i by computing their correlation. At the same time, an alignment loss is introduced to reinforce geometric consistency in RGB-D features. Next, we incorporate gradient regulation (GR) with an edge-aware loss to minimize the gradient discrepancies between the HR depth Y and the sharp-edged depth Y' . For Lagrangian duality optimization, the auxiliary alignment and edge-aware losses serve as constraint terms, seamlessly integrated with the primary reconstruction loss using Lagrangian duality theory [1, 25].

We give the details of our DuCos in the following sections. Sec. 3.1 elaborates on prompt learning and the corresponding restricted conditions. Sec. 3.2 describes the formulation of DSR as a constrained optimization problem under these restricted conditions, leading to its dual problem which is ultimately solved using Lagrangian duality theory.

3.1. Prompt Learning

Correlative Fusion. As illustrated in Fig. 2, the image branch processes the RGB input $I \in \mathbb{R}^{3 \times H \times W}$ through

a depth foundation model. A notable example is Depth Anything v2 [48], which extracts the prompt flow $F_i \in \mathbb{R}^{C \times H/p \times W/p}$ across four stages. We follow [48] to set the patch size p as 14. In the depth branch, the initial low-quality depth map undergoes upsampling by bicubic interpolation [6, 41, 53], producing the depth input $X \in \mathbb{R}^{1 \times H \times W}$. Subsequently, this input is encoded using a 3×3 convolutional head $\mathcal{F}_{\tau_1}(\cdot)$ to generate the feature representation $D_1 \in \mathbb{R}^{C \times H \times W}$, i.e.:

$$F_i = \mathcal{F}_\phi(I), \quad \text{for } 1 \leq i \leq 4; \quad (1a)$$

$$D_1 = \mathcal{F}_{\tau_1}(X), \quad (1b)$$

where $\mathcal{F}_\phi(\cdot)$ denotes the depth foundation model.

In the i -th stage, we introduce the correlative fusion module to effectively integrate the RGB-D features F_i and D_i . Specifically, the prompt F_i is resized by deconvolution and interpolation to maintain RGB-D scale consistency, resulting in $\hat{F}_i \in \mathbb{R}^{C \times H \times W}$. A residual group [52] is then applied for further feature extraction, yielding $\hat{D}_i \in \mathbb{R}^{C \times H \times W}$. This process can be denoted as:

$$\hat{F}_i = \mathcal{F}_\delta(F_i), \quad \text{for } 1 \leq i \leq 4; \quad (2a)$$

$$\hat{D}_i = \mathcal{F}_\theta(D_i), \quad (2b)$$

where $\mathcal{F}_\delta(\cdot)$ refers to the combined deconvolution and interpolation and $\mathcal{F}_\theta(\cdot)$ represents the residual group [52]. Next, we utilize the statistical measure of Pearson Correlation Coefficient to explicitly quantify the relevance between the two

features. Formally, the relevance is given by:

$$r = \frac{\sum(\hat{\mathbf{F}}_i^j - \bar{\mathbf{F}}_i)(\hat{\mathbf{D}}_i^j - \bar{\mathbf{D}}_i)}{\sqrt{\sum(\hat{\mathbf{F}}_i^j - \bar{\mathbf{F}}_i)^2} \sqrt{\sum(\hat{\mathbf{D}}_i^j - \bar{\mathbf{D}}_i)^2}}, \quad (3)$$

where $\bar{\mathbf{F}}_i$ and $\bar{\mathbf{D}}_i$ are the mean values of $\hat{\mathbf{F}}_i$ and $\hat{\mathbf{D}}_i$, respectively. j is the position index of the matrices and $r \in \mathbb{R}^C$. As we know that r is symmetric with respect to 0, where $r > 0$ indicates positive correlation and $r < 0$ signifies negative correlation. However, convolutional neural networks (CNNs) typically assign higher weight to features with high similarity and lower weight to those with less similarity instead of letting negative correlations cancel out positive ones. We thus apply a sigmoid function $\mathcal{F}_\sigma(\cdot)$ to compute the final correlation α of $\hat{\mathbf{F}}_i$ and $\hat{\mathbf{D}}_i$. Particularly, $\mathcal{F}_\sigma(\cdot)$ maps r to a more compact and nonnegative interval of $[\frac{1}{1+e}, \frac{1}{1+e^{-1}}]$. The fused result $\tilde{\mathbf{D}}_i$ is given by:

$$\alpha = \mathcal{F}_\sigma(r), \quad \beta = 1 - \alpha, \quad (4a)$$

$$\tilde{\mathbf{D}}_i = \alpha \hat{\mathbf{F}}_i + \beta \hat{\mathbf{D}}_i. \quad (4b)$$

Eq. (4b) adaptively selects regions of $\hat{\mathbf{F}}_i$ that exhibit a strong correlation with $\hat{\mathbf{D}}_i$ while preserving the original components of $\hat{\mathbf{D}}_i$ in areas with low correlation. This mechanism is especially effective for CNNs in probabilistic modeling, where negative correlation does not merely negate positive correlation but rather acts as a diminished weight in the computation. As a result, this approach effectively regulates the flow of information.

Furthermore, the iterative process involving Eqs. (2b)-(4b) refines the depth representation. Specifically, $\tilde{\mathbf{D}}_i$ from Eq. (4b) is used to update $\hat{\mathbf{D}}_i$ in Eq. (2b), and this refinement is repeated for three iterations. Afterward, a 3×3 convolution $\mathcal{F}_{\tau_2}(\cdot)$ is applied to obtain \mathbf{D}_{i+1} , which serves as the input depth feature for the subsequent CF module:

$$\mathbf{D}_{i+1} = \mathcal{F}_{\tau_2}(\tilde{\mathbf{D}}_i). \quad (5)$$

Overall, by defining $\mathcal{F}_\psi(\cdot, \cdot)$ as the complete CF module, we can unify Eqs. 1-5 into the following expression:

$$\mathbf{D}_{i+1} = \mathcal{F}_\psi(\mathbf{F}_i, \mathbf{D}_i). \quad (6)$$

Additionally, despite this fusion process, the depth feature often lacks geometric details while the prompt retains richer geometric structures. Moreover, misalignment issues persist even after resizing the prompt to match the resolution of the depth feature. To mitigate these challenges, we introduce a simple yet effective constraint designed to enhance geometric consistency:

$$\mathcal{L}_{cf} = \frac{1}{n} \|\mathcal{H}(\tilde{\mathbf{D}}_i) - \mathcal{H}(\hat{\mathbf{F}}_i)\|_2^2, \quad (7)$$

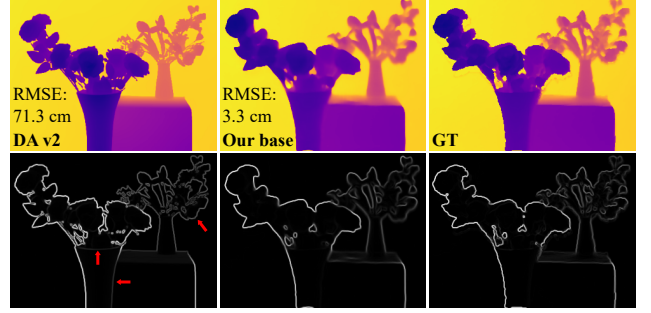


Figure 3. Visual comparisons of foundation models and traditional DSR methods. DA v2: Depth Anything v2 [48] (ViT-L encoder).

where $\mathcal{H}(\cdot)$ denotes a combination of a 1×1 convolution followed by normalization. It reduces the features to a single channel and normalizes them to the range $[0, 1]$. n is the number of valid pixels.

Finally, given the fused feature $\mathbf{D}_4 \in \mathbb{R}^{C \times H \times W}$ produced from the fourth CF module, we conduct a 3×3 convolutional tail $\mathcal{F}_{\tau_3}(\cdot)$ to map the channel C to 1, yielding the final depth prediction:

$$\mathbf{Y} = \mathcal{F}_{\tau_3}(\mathbf{D}_4). \quad (8)$$

Gradient Regulation. As shown in Fig. 2, the image branch utilizing a foundation model also produces a depth prediction denoted as \mathbf{Y}' . However, monocular depth estimation is inherently an ill-posed problem since models can only infer the relative depth instead of absolute measurements. Fortunately, as shown in Fig. 3, the visual quality of \mathbf{Y}' remains remarkably high despite its significant error. Notably, \mathbf{Y}' exhibits exceptional clarity and sharp gradient, even surpassing the ground truth depth.

In view of the large discrepancy between the depth values of \mathbf{Y}' and the target \mathbf{Y} , directly fusing these results is not appropriate. Instead, we utilize the gradient representation of \mathbf{Y}' as a constraint to regulate its edges. Specifically, we first adjust the depth discrepancy using Min-Max Normalization $\mathcal{N}(\cdot)$. We then calculate the first derivative to get their gradient representations:

$$\mathcal{G}(\mathbf{Y}) = \sqrt{\left(\frac{\partial \mathcal{N}(\mathbf{Y})}{\partial x}\right)^2 + \left(\frac{\partial \mathcal{N}(\mathbf{Y})}{\partial y}\right)^2}, \quad (9a)$$

$$\mathcal{G}(\mathbf{Y}') = \sqrt{\left(\frac{\partial \mathcal{N}(\mathbf{Y}')}{\partial x}\right)^2 + \left(\frac{\partial \mathcal{N}(\mathbf{Y}')}{\partial y}\right)^2}. \quad (9b)$$

Subsequently, we propagate the edge priors from the depth foundation model by minimizing their normalized gradient distances through:

$$\mathcal{L}_{gr} = \frac{1}{n} \|\mathcal{G}(\mathbf{Y}) - \mathcal{G}(\mathbf{Y}')\|_1. \quad (10)$$

This constraint allows us to improve the sharpness and overall quality of our estimated depth maps.

3.2. Lagrangian Duality Optimization

Given the HR depth prediction \mathbf{Y} and the ground truth \mathbf{Z} , we use the commonly adopted reconstruction loss [6, 24, 44] for optimization:

$$\mathcal{L}_{rec} = \frac{1}{n} \|\mathbf{Y} - \mathbf{Z}\|_1. \quad (11)$$

By integrating Eq. (11) with the two prompts from Eq. (7) and Eq. (10), we can further enhance the optimization of the target depth. Unlike previous DSR methods [36, 37, 41, 54] that introduce additional loss terms as auxiliary constraints, we adopt the Lagrangian duality theory [1, 25] to translate the optimization problem into a constrained form. Specifically, based on Eqs. (7) and (10), the *primal problem* can be written as:

$$\min_{\omega} \mathcal{L}_{rec}, \quad \text{s.t. } \mathcal{L}_{cf} < \varepsilon_1, \mathcal{L}_{gr} < \varepsilon_2, \quad (12)$$

where ω indicates the network weight of our DuCos. ε_1 and ε_2 are small positive values approaching zero, signifying that errors have become negligible. Next, we introduce two Lagrangian multipliers λ and μ to formulate the Lagrangian function as:

$$\begin{aligned} \mathcal{L}(\omega, \lambda, \mu) &= \underbrace{\mathcal{L}_{rec}}_{\text{target}} + \underbrace{\lambda \mathcal{L}_{cf} + \mu \mathcal{L}_{gr}}_{\text{Lag. const. term}} \\ &= \frac{1}{n} \|\mathbf{Y} - \mathbf{Z}\|_1 + \frac{\lambda}{n} \|\mathcal{H}(\tilde{\mathbf{D}}_i) - \mathcal{H}(\hat{\mathbf{F}}_i)\|_2^2 \\ &\quad + \frac{\mu}{n} \|\mathcal{G}(\mathbf{Y}) - \mathcal{G}(\mathbf{Y}')\|_1, \end{aligned} \quad (13)$$

where $\lambda \geq 0$ and $\mu \geq 0$ according to the Karush-Kuhn-Tucker (KKT) conditions [15]. We then minimize the Lagrangian function to get the dual function:

$$\mathcal{D}(\lambda, \mu) = \min_{\omega} \mathcal{L}(\omega, \lambda, \mu). \quad (14)$$

Subsequently, the *dual problem* corresponding to the primal problem in Eq. (12) is formulated by maximizing Eq. (14):

$$\max_{\lambda, \mu} \mathcal{D}(\lambda, \mu) = \max_{\lambda, \mu} \min_{\omega} \mathcal{L}(\omega, \lambda, \mu). \quad (15)$$

The dual optimization in Eq. (15) consists of two key steps: **Step 1.** Fix λ and μ , minimize the Lagrangian function to obtain the optimal network weight:

$$\omega^*(\lambda, \mu) = \arg \min_{\omega} (\mathcal{L}_{rec} + \lambda \mathcal{L}_{cf} + \mu \mathcal{L}_{gr}). \quad (16)$$

Step 2. Adjust λ and μ , maximize the dual function:

$$\lambda^*, \mu^* = \arg \max_{\lambda, \mu} \mathcal{D}(\lambda, \mu). \quad (17)$$

Alg. 1 gives the details of the dual problem optimization in Eq. (15). The Lagrangian duality optimization allows for the flexible integration of multiple constraint conditions and reconstruction objectives. The optimization process is simplified by relaxing the constraints, providing an exact solution when the loss function is convex and an approximate solution when the loss function is non-convex.

Algorithm 1: Dual Problem Solving

Input: $\mathbf{Y}, \mathbf{Z}, \tilde{\mathbf{D}}_i, \hat{\mathbf{F}}_i, \mathbf{Y}'$

- 1 Initialize learning rate $\eta_{\omega} = 1e-5$, $\lambda = 0.01$, $\mu = 0.05$, step-length $\eta_{\lambda} = \eta_{\mu} = 0.01$
 - 2 Set maximum epoch T
 - 3 **for** epoch $t = 1$ to T **do**
 - 4 **Step 1: Fix λ and μ , optimize ω**
 - 5 Total Lag. loss: $\mathcal{L}(\omega, \lambda, \mu) = \mathcal{L}_{rec} + \lambda \mathcal{L}_{cf} + \mu \mathcal{L}_{gr}$
 - 6 Gradients of ω : $\nabla_{\omega} \mathcal{L}(\omega, \lambda, \mu)$
 - 7 Update ω : $\omega \leftarrow \omega - \eta_{\omega} \nabla_{\omega} \mathcal{L}(\omega, \lambda, \mu)$
 - 8 **Step 2: Optimize λ and μ**
 - 9 Update $\eta_{\lambda}, \eta_{\mu}$: $\eta_{\lambda} \leftarrow \eta_{\lambda} (1 - \frac{t}{T})$, $\eta_{\mu} \leftarrow \eta_{\mu} (1 - \frac{t}{T})$
 - 10 Update λ, μ : $\lambda \leftarrow \lambda + \eta_{\lambda} \mathcal{L}_{cf}$, $\mu \leftarrow \mu + \eta_{\mu} \mathcal{L}_{gr}$
 - 11 Ensure λ, μ to satisfy KKT conditions:
 - 12 $\lambda \leftarrow \text{clamp}(\lambda, \min = 0)$, $\mu \leftarrow \text{clamp}(\mu, \min = 0)$
 - 13 **end for**
- Output:** Optimized parameters ω, λ, μ
-

4. Experiment

4.1. Dataset

With the advancement of computer vision, training with synthetic data has become a crucial approach to reducing data acquisition costs. Thus, we retrain all methods on the fully synthetic Hypersim [31] dataset and evaluate them on the test sets of various DSR datasets: TOFDSR [45], RGB-D-D [6], NYUv2 [34], Middlebury [7, 32], and Lu [22]. The high-quality RGB-D data of Hypersim are synthesized from 77,400 images across 461 indoor scenes, offering per-pixel geometric labels along with comprehensive scene geometry, material properties, and lighting information. For DSR training, we choose 2,000 RGB-D pairs. Building on previous approaches [6, 53, 54], we use bicubic interpolation to generate LR depth from depth annotations across these five datasets. Additionally, TOFDSR and RGB-D-D also provide real-world LR depth data, enabling the evaluation of the generalization capabilities of the different models. Refer to our appendix for metrics and implementation details.

4.2. Comparison with State-of-the-arts

Synthetic DSR. We first evaluate our proposed DuCos on widely used synthetic DSR datasets. As shown in Tab. 1, DuCos consistently delivers superior or highly competitive performance on various datasets and scales. Particularly, in the $\times 2$ case, our DuCos achieves the lowest RMSE and MAE while maintaining the highest δ_1 , outperforming second-best methods by an average of 29.1% in RMSE and 29.6% in MAE on all five datasets. Likewise, in the case of $\times 4$, our DuCos continues to demonstrate its superiority, exceeding the second-best approaches by 14.9% in RMSE and 24.1% in MAE, respectively. As the scale increases to $\times 8$ and $\times 16$, the performance of all methods naturally degrades due to the loss of information in depth maps with

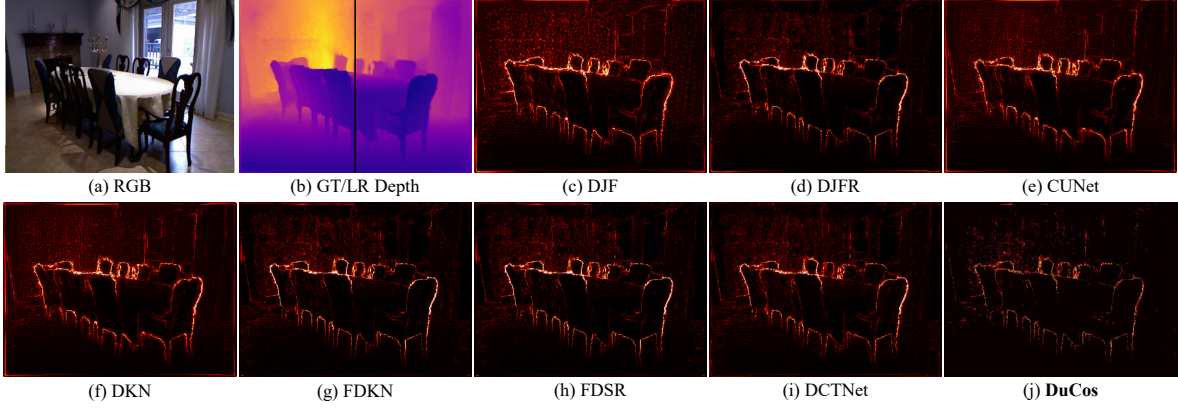


Figure 4. Error map comparisons on the synthetic NYU v2 dataset ($\times 4$), where warmer colors indicate higher errors.

Method	Scale	Middlebury			Lu			NYU v2			RGB-D-D			TOFDSR		
		RMSE	MAE	δ_1	RMSE	MAE	δ_1	RMSE	MAE	δ_1	RMSE	MAE	δ_1	RMSE	MAE	δ_1
DJF [16]	$\times 2$	1.14	0.63	98.56	1.08	0.44	99.00	2.32	0.83	99.49	1.18	0.36	99.64	2.99	0.66	98.74
DJFR [17]		1.22	0.58	98.42	1.39	0.45	98.94	1.87	0.51	99.68	0.98	0.27	99.74	1.58	0.28	99.57
CUNet [5]		1.01	0.58	98.78	1.06	0.50	99.10	<u>1.50</u>	<u>0.46</u>	<u>99.81</u>	<u>0.84</u>	0.25	<u>99.81</u>	1.69	0.33	99.49
FDKN [13]		1.35	0.62	98.39	1.59	0.49	98.91	2.05	0.50	99.63	1.04	0.26	99.70	1.85	0.36	99.32
DKN [13]		1.32	0.62	98.48	1.48	0.48	99.00	1.95	0.49	99.66	0.98	<u>0.24</u>	99.74	1.87	0.36	99.33
FDSR [6]		<u>0.94</u>	<u>0.51</u>	98.89	<u>0.94</u>	<u>0.39</u>	99.14	1.74	0.57	99.70	0.91	0.26	99.76	1.55	0.40	99.24
DCTNet [53]		1.01	0.53	<u>98.90</u>	1.03	0.59	<u>99.36</u>	1.59	0.59	99.76	0.89	0.28	99.79	<u>0.80</u>	<u>0.23</u>	<u>99.87</u>
DADA [24]		1.28	0.60	98.47	1.45	0.48	99.07	2.00	0.54	99.65	1.04	0.27	99.71	1.73	0.37	99.26
DuCos		0.81	0.46	99.28	0.65	0.26	99.68	1.20	0.37	99.88	0.74	0.22	99.85	0.52	0.13	99.94
DJF [16]		$\times 4$	1.93	1.11	97.11	1.93	1.11	98.20	3.60	1.67	99.05	1.63	0.74	99.39	3.75	1.14
DJFR [17]	1.83		1.04	96.91	1.85	1.02	98.36	3.27	1.14	99.04	1.54	0.48	99.35	2.97	0.58	99.00
CUNet [5]	<u>1.61</u>		0.98	97.79	<u>1.73</u>	0.97	98.48	3.22	1.44	99.21	1.52	0.65	99.43	3.57	1.13	98.19
FDKN [13]	1.80		0.80	97.69	2.11	0.58	98.53	3.28	0.93	99.28	1.56	0.42	99.42	2.80	0.58	98.96
DKN [13]	1.77		0.78	97.77	2.05	<u>0.56</u>	<u>98.58</u>	3.15	0.90	99.34	1.50	0.41	99.49	2.73	0.56	99.04
FDSR [6]	1.72		0.84	97.69	1.95	<u>0.56</u>	98.52	2.94	<u>0.85</u>	<u>99.39</u>	<u>1.41</u>	<u>0.40</u>	<u>99.51</u>	<u>2.41</u>	<u>0.51</u>	<u>99.07</u>
DCTNet [53]	1.66		<u>0.77</u>	<u>97.86</u>	1.85	0.57	98.56	<u>2.90</u>	0.99	<u>99.37</u>	1.49	0.44	99.45	2.86	0.59	98.98
DADA [24]	1.82		0.83	97.45	2.12	0.66	98.35	3.08	0.96	99.33	1.63	0.46	99.39	2.85	0.68	98.57
DuCos	1.45		0.68	98.30	1.38	0.41	99.08	2.60	0.81	99.49	1.27	0.36	99.60	2.09	0.33	99.58
DJF [16]	$\times 8$		3.09	1.46	94.10	3.58	1.22	95.60	5.56	2.30	97.70	2.58	0.96	98.29	5.59	1.71
DJFR [17]		2.82	1.25	95.31	3.24	1.07	95.86	5.20	1.94	98.21	2.61	0.93	98.25	5.11	1.35	97.16
CUNet [5]		2.86	1.46	94.44	2.85	1.25	96.32	5.50	2.23	97.78	2.35	0.92	98.60	5.14	1.64	96.67
FDKN [13]		2.51	1.13	<u>96.26</u>	2.67	<u>0.85</u>	<u>97.39</u>	4.93	<u>1.67</u>	<u>98.65</u>	<u>2.25</u>	<u>0.70</u>	<u>98.86</u>	<u>4.40</u>	0.96	<u>98.15</u>
DKN [13]		2.43	<u>1.12</u>	<u>96.26</u>	2.88	0.88	97.13	4.88	1.71	98.62	2.33	0.74	98.76	4.54	1.06	97.87
FDSR [6]		<u>2.41</u>	1.13	96.24	<u>2.69</u>	0.86	97.35	<u>4.82</u>	1.69	98.57	<u>2.25</u>	0.73	98.72	4.28	<u>0.95</u>	98.06
DCTNet [53]		2.75	1.31	95.25	3.07	1.18	96.38	4.90	2.12	98.28	2.47	0.92	98.60	5.38	1.57	97.01
DADA [24]		2.77	1.27	95.01	3.76	1.17	96.01	4.83	1.86	98.34	2.81	0.93	98.29	5.86	1.64	96.15
DuCos		2.23	0.97	97.07	2.67	0.72	97.86	4.61	1.52	98.86	2.23	0.66	98.89	4.60	0.92	98.30
DJF [16]		$\times 16$	5.50	2.92	84.66	6.53	2.69	88.91	9.82	4.73	93.05	4.46	2.04	94.99	8.19	3.49
DJFR [17]	5.16		2.61	86.39	6.46	2.38	89.66	9.50	4.28	93.63	4.36	1.84	95.48	8.06	3.06	92.20
CUNet [5]	4.72		2.40	88.45	5.63	2.17	91.33	8.63	3.88	94.55	3.81	1.58	96.36	7.36	2.73	93.40
FDKN [13]	4.42		2.10	90.80	5.48	1.91	92.24	7.97	3.43	95.76	3.71	1.45	96.81	7.16	2.29	94.78
DKN [13]	4.17		1.97	91.67	5.44	1.90	91.94	7.70	3.28	96.06	<u>3.70</u>	1.39	97.06	7.24	2.20	95.26
FDSR [6]	<u>3.97</u>		<u>1.81</u>	<u>92.52</u>	<u>5.23</u>	<u>1.67</u>	<u>93.44</u>	7.29	<u>2.91</u>	<u>96.86</u>	3.44	<u>1.24</u>	<u>97.37</u>	6.85	<u>1.91</u>	<u>95.96</u>
DCTNet [53]	5.07		2.59	86.91	5.83	2.25	90.19	9.10	4.24	94.04	4.13	1.66	96.30	8.04	2.77	93.45
DADA [24]	4.11		2.06	90.09	6.19	2.22	90.95	7.99	3.54	95.64	4.01	1.59	96.71	7.79	2.70	93.25
DuCos	3.96		1.69	93.52	5.18	1.59	93.89	<u>7.37</u>	2.82	97.12	3.44	1.16	97.61	<u>6.90</u>	1.77	96.51

Table 1. Quantitative comparisons on the synthetic DSR benchmarks. The **best** and second-best results are highlighted.

lower resolution. However, DuCos remains highly effective, preserving lower errors and higher accuracy. Fig. 4 provides a visual comparison with the latest approaches, where the error maps highlight the ability of our DuCos to reconstruct depth with higher precision and thus capturing more accurate boundaries.

Arbitrary-scale DSR. In downstream applications, scaling factors are often variable or unknown. In addition to evaluating DSR methods at fixed integer scales, we thus also

assess their performance on arbitrary scaling factors. As illustrated in Fig. 5, experiments are conducted at $\times 1.5$, $\times 2.7$, $\times 3.4$, $\times 5.3$, and $\times 11.6$ scales. Our DuCos consistently achieves outstanding results across all scales and datasets. Specifically, compared to all methods on these five scales, DuCos demonstrates significantly superior performance on RMSE, MAE, and δ_1 , with average improvements of 20.6%, 22.3%, and 0.47 percent points, respectively. These results further validate DuCos’s effectiveness.

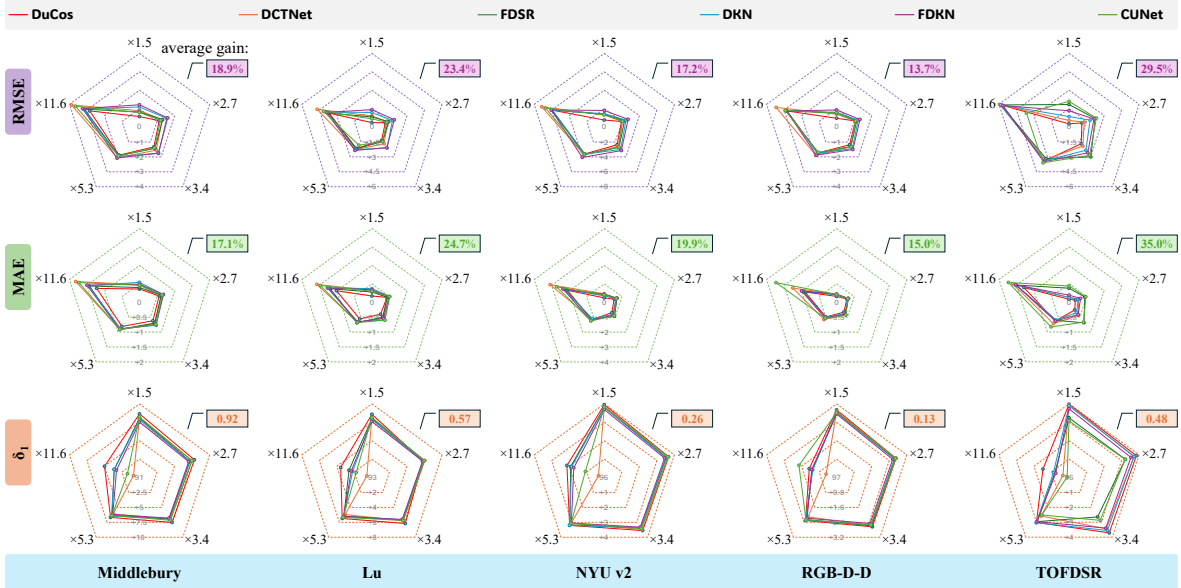


Figure 5. Comparisons with arbitrary scaling factors on the synthetic DSR datasets. Refer to our appendix for more details.

Method	RGB-D-D			TOFDSR			RGB-D-D w/ noise			TOFDSR w/ noise		
	RMSE	MAE	δ_1	RMSE	MAE	δ_1	RMSE	MAE	δ_1	RMSE	MAE	δ_1
DJF [16]	5.54	3.43	93.81	5.84	2.13	96.79	7.94	5.16	84.82	11.45	7.87	67.95
DJFR [17]	5.52	3.51	93.58	5.72	2.10	97.03	7.50	4.83	86.25	10.92	7.39	70.46
CUNet [5]	5.84	3.06	94.75	6.04	2.21	96.46	6.69	4.14	89.36	9.76	5.86	80.43
FDKN [13]	5.37	2.70	96.05	5.77	2.19	97.33	6.66	4.26	90.09	8.13	4.66	86.24
DKN [13]	5.08	2.58	96.28	5.50	2.07	97.54	6.50	4.16	90.04	7.42	4.29	88.20
FDSR [6]	5.49	3.10	94.77	5.03	1.67	<u>97.61</u>	6.39	4.07	90.69	6.31	3.17	92.74
DCTNet [53]	5.43	3.29	93.15	5.16	2.10	<u>96.37</u>	6.04	<u>3.79</u>	<u>90.90</u>	7.52	4.50	86.04
SFG [51]	<u>3.88</u>	<u>1.96</u>	<u>97.09</u>	<u>4.52</u>	<u>1.72</u>	97.45	<u>5.87</u>	<u>3.79</u>	89.84	<u>5.46</u>	<u>2.89</u>	<u>93.02</u>
DuCos	3.68	1.54	97.87	4.29	1.15	98.67	4.14	2.00	96.76	5.20	2.20	96.44

Table 2. Quantitative comparisons on the real-world DSR datasets, including RGB-D-D, TOFDSR and their noisy patterns.

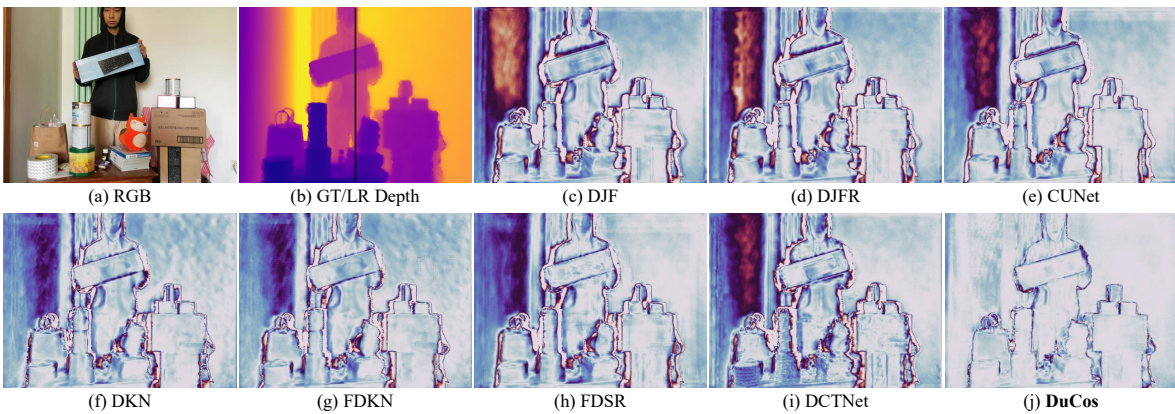


Figure 6. Error map comparisons on the real-world RGB-D-D dataset. Please see our appendix for more visualizations.

Real-world DSR. Since the introduction of FDSR [6], real-world DSR has gained increasing attention. Unlike integer or arbitrary scaling, the real-world setting reflects the practical challenges of DSR. Additionally, we assess model robustness by introducing noise to simulate external disturbances. As listed in Tab. 2, DuCos consistently outperforms all competing methods on both datasets. It surpasses the

second-best SFG by 4.2 mm in MAE on RGB-D-D, and exceeds SFG by 5.7 mm on TOFDSR. Even under noisy conditions², our DuCos maintains its advantage. On average, DuCos outperforms the suboptimal methods by 17.1% in RMSE, 35.6% in MAE, and 4.6 points in δ_1 , demonstrating

²Following SFG [51], we applied Gaussian blur (standard deviation: 3.6) and Gaussian noise (mean: 0, standard deviation: 0.07) to LR depth.

Method	NYU v2			RGB-D-D			TOFDSR		
	RMSE	MAE	$\delta_{1.05}$	RMSE	MAE	$\delta_{1.05}$	RMSE	MAE	$\delta_{1.05}$
DJF [16]	119.41	101.14	8.53	34.48	29.93	16.26	47.98	44.30	10.94
DJFR [17]	147.43	121.73	7.85	40.46	34.49	14.03	50.14	45.81	8.59
CUNet [5]	133.90	108.96	7.14	35.03	30.67	15.08	50.25	46.53	8.96
FDKN [13]	187.53	154.15	4.26	42.37	36.91	14.04	49.34	44.88	14.28
DKN [13]	186.10	152.74	4.33	40.38	35.15	14.40	47.27	43.34	9.58
FDSR [6]	118.76	101.28	8.39	35.88	30.15	20.64	45.96	40.92	20.26
DCTNet [53]	118.45	101.30	8.20	37.85	33.25	12.82	51.58	48.41	6.88
DuCos	58.74	46.00	26.19	24.64	21.13	26.45	30.40	25.63	22.37

Table 3. Quantitative comparisons of compressed DSR on NYU v2, RGB-D-D, and TOFDSR datasets.

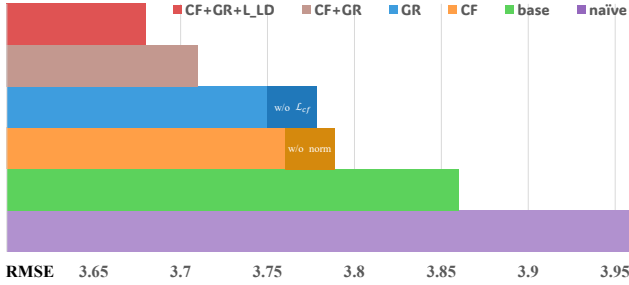


Figure 7. Ablation study of DuCos on the real-world RGB-D-D.

strong robustness against noise. Fig. 6 shows that DuCos recovers a higher-quality depth map near the boundaries and textureless areas.

Compressed DSR. Due to the limitations of consumer-grade depth cameras and bandwidth constraints, restoring accurate depth from compressed sources is crucial. Following GDNet [55], Tab. 3 presents the $\times 8$ results. Our DuCos consistently outperforms all previous methods, achieving average improvements of 37.6% in RMSE, 40.4% in MAE, and 8.5 points in δ_1 over the second-best methods. These significant improvements underscore the effectiveness and generalization of our approach in minimizing reconstruction error while substantially enhancing accuracy.

4.3. Ablation Study

DuCos designs. Fig. 7 presents the ablation results on the real-world RGB-D-D. The naïve model consists of separate image and depth branches, each using four residual groups [52] for feature extraction and fused by element-wise addition. Our introduction of depth foundation models as prompts reduces the RMSE from 3.97 cm to 3.86 cm. Based on this, CF improves performance by 0.1 cm, while GR yields a 0.11 cm improvement. Furthermore, combining CF and GR reduces the error of the base model by 0.15 cm. Finally, our Lagrangian duality strategy contributes to the best performance, achieving an RMSE of 3.68 cm. Notably, the alignment loss \mathcal{L}_{cf} in CF also leads to performance gains, reducing the RMSE from 3.82 cm to 3.76 cm. Additionally, normalization in GR mitigates discrepancies between the target depth and the relative depth from the foundation models, further reducing the error by 0.05 cm. In summary, each component contributes positively to the entire model.

Prompt in DuCos	Params.	Time	NYU v2			Middlebury		
	(M)	(ms)	RMSE	MAE	$\delta_{1.05}$	RMSE	MAE	$\delta_{1.05}$
DepthFormer [18]	282.76	58.47	7.27	2.82	97.12	4.01	1.74	93.21
UniDepth v2-S [29]	87.21	91.27	8.69	3.30	96.12	4.21	1.79	93.12
UniDepth v2-L [29]	372.97	159.28	8.86	3.45	95.85	5.40	2.37	89.83
DA v2-S [48]	34.38	23.53	7.37	2.82	97.12	3.96	1.69	93.52
DA v2-B [48]	107.19	31.24	7.34	2.79	97.14	3.94	1.69	93.61
DA v2-L [48]	345.06	71.81	7.15	2.74	97.29	3.64	1.55	94.35

Table 4. Ablation study of DuCos with different foundation models on the synthetic NYU v2 ($\times 16$) and Middlebury ($\times 16$).

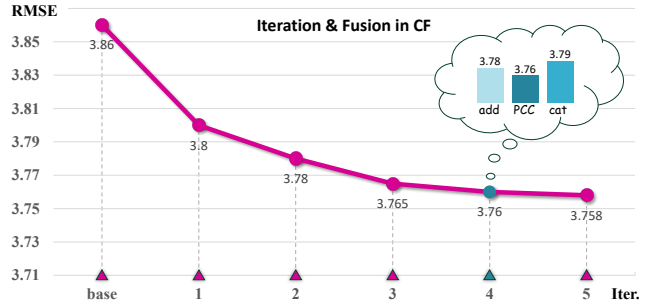


Figure 8. Ablation study of CF on the real-world RGB-D-D.

Iteration & fusion in CF. Fig. 8 shows the ablation study of the CF module. As the number of iterations increases, the error progressively decreases. To balance performance and computational complexity, we set the default iteration count to 4. Furthermore, our findings indicate that the fusion based on the Pearson correlation coefficient (PCC) outperforms both addition and concatenation, achieving improvements of 0.02 cm and 0.03 cm, respectively.

Depth Foundation Models. Tab. 4 lists the ablation study of DuCos using different foundation models as prompts, including DepthFormer [18], UniDepth v2 [29], and DA v2 [48]. The inference time is measured on a single 4090 GPU. The results indicate that heavier prompts generally yield better performance than their smaller counterparts. Among these models, DA v2-L achieves the highest performance. Considering the complexity-performance trade-off, we adopt DA v2-S as the default prompt for DuCos.

5. Conclusion

In this paper, we introduce DuCos, a novel DSR paradigm based on Lagrangian duality theory. By formulating DSR as a constrained optimization problem, our DuCos can restore global reconstruction with local geometric consistency, leading to better depth predictions. Furthermore, we pioneer the use of foundation models as prompts, leveraging correlative fusion and gradient regulation to enhance generalization across diverse scenarios. These prompts are seamlessly incorporated into the Lagrangian constraint term, creating a synergistic framework that combines theoretical rigor with practical adaptability. Extensive experiments demonstrate the superiority of our DuCos in terms of accuracy, robustness, and generalization.

References

- [1] Stephen Boyd. Convex optimization. *Cambridge UP*, 2004. 1, 3, 5
- [2] Xuanhong Chen, Hang Wang, Jialiang Chen, Kairui Feng, Jinfan Liu, Xiaohang Wang, Weimin Zhang, and Bingbing Ni. Intrinsic phase-preserving networks for depth super-resolution. In *AAAI*, pages 1210–1218, 2024. 2
- [3] Runmin Cong, Ronghui Sheng, Hao Wu, Yulan Guo, Yunchao Wei, Wangmeng Zuo, Yao Zhao, and Sam Kwong. Learning hierarchical color guidance for depth map super-resolution. *IEEE Transactions on Instrumentation and Measurement*, 2024. 2
- [4] Riccardo De Lutio, Alexander Becker, Stefano D’Aronco, Stefania Russo, Jan D Wegner, and Konrad Schindler. Learning graph regularisation for guided super-resolution. In *CVPR*, pages 1979–1988, 2022. 1
- [5] Xin Deng and Pier Luigi Dragotti. Deep convolutional neural network for multi-modal image restoration and fusion. *IEEE Transactions on Pattern Analysis and Machine Intelligence*, 43(10):3333–3348, 2020. 6, 7, 8, 1, 2
- [6] Lingzhi He, Hongguang Zhu, Feng Li, Huihui Bai, Runmin Cong, Chunjie Zhang, Chunyu Lin, Meiqin Liu, and Yao Zhao. Towards fast and accurate real-world depth super-resolution: Benchmark dataset and baseline. In *CVPR*, pages 9229–9238, 2021. 1, 2, 3, 5, 6, 7, 8
- [7] Heiko Hirschmuller and Daniel Scharstein. Evaluation of cost functions for stereo matching. In *CVPR*, pages 1–8, 2007. 5
- [8] Mu Hu, Wei Yin, Chi Zhang, Zhipeng Cai, Xiaoxiao Long, Hao Chen, Kaixuan Wang, Gang Yu, Chunhua Shen, and Shaojie Shen. Metric3d v2: A versatile monocular geometric foundation model for zero-shot metric depth and surface normal estimation. *arXiv preprint arXiv:2404.15506*, 2024. 2
- [9] Tak-Wai Hui, Chen Change Loy, and Xiaoou Tang. Depth map super-resolution by deep multi-scale guidance. In *ECCV*, pages 353–369, 2016. 2
- [10] Hualie Jiang, Zhiqiang Lou, Laiyan Ding, Rui Xu, Minglang Tan, Wenjie Jiang, and Rui Huang. Defom-stereo: Depth foundation model based stereo matching. *arXiv preprint arXiv:2501.09466*, 2025. 2
- [11] Jiahui Kang, Qing Cai, Runqing Tan, Yimei Liu, and Zhi Liu. C2pd: Continuity-constrained pixelwise deformation for guided depth super-resolution. *arXiv preprint arXiv:2501.07688*, 2025. 2
- [12] Bingxin Ke, Anton Obukhov, Shengyu Huang, Nando Metzger, Rodrigo Caye Daudt, and Konrad Schindler. Repurposing diffusion-based image generators for monocular depth estimation. In *CVPR*, pages 9492–9502, 2024. 2
- [13] Beomjun Kim, Jean Ponce, and Bumsu Ham. Deformable kernel networks for joint image filtering. *International Journal of Computer Vision*, 129(2):579–600, 2021. 1, 2, 6, 7, 8
- [14] Diederik P Kingma. Adam: A method for stochastic optimization. *arXiv preprint arXiv:1412.6980*, 2014. 1
- [15] Harold W. Kuhn and Albert W. Tucker. Nonlinear programming. In *Proceedings of the Second Berkeley Symposium on Mathematical Statistics and Probability*, pages 481–492. University of California Press, 1951. 5
- [16] Yijun Li, Jia-Bin Huang, Narendra Ahuja, and Ming-Hsuan Yang. Deep joint image filtering. In *ECCV*, pages 154–169, 2016. 6, 7, 8
- [17] Yijun Li, Jia-Bin Huang, Narendra Ahuja, and Ming-Hsuan Yang. Joint image filtering with deep convolutional networks. *IEEE Transactions on Pattern Analysis and Machine Intelligence*, 41(8):1909–1923, 2019. 2, 6, 7, 8
- [18] Zhenyu Li, Zehui Chen, Xianming Liu, and Junjun Jiang. Depthformer: Exploiting long-range correlation and local information for accurate monocular depth estimation. *Machine Intelligence Research*, 20(6):837–854, 2023. 8
- [19] Haotong Lin, Sida Peng, Jingxiao Chen, Songyou Peng, Jiaming Sun, Minghuan Liu, Hujun Bao, Jiashi Feng, Xiaowei Zhou, and Bingyi Kang. Prompting depth anything for 4k resolution accurate metric depth estimation. *arXiv preprint arXiv:2412.14015*, 2024. 2
- [20] Lahav Lipson, Zachary Teed, and Jia Deng. Raft-stereo: Multilevel recurrent field transforms for stereo matching. In *3DV*, pages 218–227. IEEE, 2021. 2
- [21] Zhiheng Liu, Ka Leong Cheng, Qiuyu Wang, Shuzhe Wang, Hao Ouyang, Bin Tan, Kai Zhu, Yujun Shen, Qifeng Chen, and Ping Luo. Depthlab: From partial to complete. *arXiv preprint arXiv:2412.18153*, 2024. 2
- [22] Si Lu, Xiaofeng Ren, and Feng Liu. Depth enhancement via low-rank matrix completion. In *CVPR*, pages 3390–3397, 2014. 5
- [23] Rémi Marsal, Alexandre Chapoutot, Philippe Xu, and David Filliat. Foundation models meet low-cost sensors: Test-time adaptation for rescaling disparity for zero-shot metric depth estimation. *arXiv preprint arXiv:2412.14103*, 2024. 2
- [24] Nando Metzger, Rodrigo Caye Daudt, and Konrad Schindler. Guided depth super-resolution by deep anisotropic diffusion. In *CVPR*, pages 18237–18246, 2023. 1, 2, 5, 6
- [25] D. P. Palomar and M. Chiang. A tutorial on lagrangian duality and decomposition in optimization. *IEEE Transactions on Signal Processing*, 54(3):1177–1193, 2006. 1, 3, 5
- [26] Jinshan Pan, Jiangxin Dong, Jimmy S Ren, Liang Lin, Jinhui Tang, and Ming-Hsuan Yang. Spatially variant linear representation models for joint filtering. In *CVPR*, pages 1702–1711, 2019. 1, 2
- [27] Jin-Hwi Park and Hae-Gon Jeon. A simple yet universal framework for depth completion. In *NeurIPS*, 2024. 2
- [28] Jin-Hwi Park, Chanhwi Jeong, Junoh Lee, and Hae-Gon Jeon. Depth prompting for sensor-agnostic depth estimation. In *CVPR*, pages 9859–9869, 2024. 2
- [29] Luigi Piccinelli, Yung-Hsu Yang, Christos Sakaridis, Mattia Segu, Siyuan Li, Luc Van Gool, and Fisher Yu. Unidepth: Universal monocular metric depth estimation. In *CVPR*, pages 10106–10116, 2024. 2, 8
- [30] Gernot Riegler, Matthias Rüther, and Horst Bischof. Atgnet: Accurate depth super-resolution. In *ECCV*, pages 268–284, 2016. 2
- [31] Mike Roberts, Jason Ramapuram, Anurag Ranjan, Atulit Kumar, Miguel Angel Bautista, Nathan Paczan, Russ Webb,

- and Joshua M Susskind. Hypersim: A photorealistic synthetic dataset for holistic indoor scene understanding. In *ICCV*, pages 10912–10922, 2021. 5, 1, 2
- [32] Daniel Scharstein and Chris Pal. Learning conditional random fields for stereo. In *CVPR*, pages 1–8, 2007. 5
- [33] Wuxuan Shi, Mang Ye, and Bo Du. Symmetric uncertainty-aware feature transmission for depth super-resolution. In *ACMMM*, pages 3867–3876, 2022. 1
- [34] Nathan Silberman, Derek Hoiem, Pushmeet Kohli, and Rob Fergus. Indoor segmentation and support inference from rgbd images. In *ECCV*, pages 746–760, 2012. 5
- [35] Hang Su, Varun Jampani, Deqing Sun, Orazio Gallo, Erik Learned-Miller, and Jan Kautz. Pixel-adaptive convolutional neural networks. In *CVPR*, pages 11166–11175, 2019. 1
- [36] Baoli Sun, Xinchen Ye, Baopu Li, Haojie Li, Zhihui Wang, and Rui Xu. Learning scene structure guidance via cross-task knowledge transfer for single depth super-resolution. In *CVPR*, pages 7792–7801, 2021. 1, 5
- [37] Qi Tang, Runmin Cong, Ronghui Sheng, Lingzhi He, Dan Zhang, Yao Zhao, and Sam Kwong. Bridgenet: A joint learning network of depth map super-resolution and monocular depth estimation. In *ACM MM*, pages 2148–2157, 2021. 2, 5
- [38] Massimiliano Viola, Kevin Qu, Nando Metzger, Bingxin Ke, Alexander Becker, Konrad Schindler, and Anton Obukhov. Marigold-dc: Zero-shot monocular depth completion with guided diffusion. *arXiv preprint arXiv:2412.13389*, 2024. 2
- [39] Haotian Wang, Meng Yang, Ce Zhu, and Nanning Zheng. Rgb-guided depth map recovery by two-stage coarse-to-fine dense crf models. *IEEE Transactions on Image Processing*, 32:1315–1328, 2023. 1
- [40] Zhengxue Wang and Zhiqiang Yan. Degradation oriented and regularized network for real-world depth super-resolution. *arXiv e-prints*, pages arXiv–2410, 2024. 2
- [41] Zhengxue Wang, Zhiqiang Yan, and Jian Yang. Sgnet: Structure guided network via gradient-frequency awareness for depth map super-resolution. In *AAAI*, pages 5823–5831, 2024. 1, 2, 3, 5
- [42] Zhengxue Wang, Zhiqiang Yan, Ming-Hsuan Yang, Jinshan Pan, Jian Yang, Ying Tai, and Guangwei Gao. Scene prior filtering for depth map super-resolution. *arXiv preprint arXiv:2402.13876*, 2024. 2
- [43] Bowen Wen, Matthew Trepte, Joseph Aribido, Jan Kautz, Orazio Gallo, and Stan Birchfield. Foundationstereo: Zero-shot stereo matching. *arXiv e-prints*, pages arXiv–2501, 2025. 2
- [44] Zhiqiang Yan, Kun Wang, Xiang Li, Zhenyu Zhang, Guangyu Li, Jun Li, and Jian Yang. Learning complementary correlations for depth super-resolution with incomplete data in real world. *IEEE Transactions on Neural Networks and Learning Systems*, 35(4):5616–5626, 2022. 1, 5
- [45] Zhiqiang Yan, Yuankai Lin, Kun Wang, Yupeng Zheng, Yufei Wang, Zhenyu Zhang, Jun Li, and Jian Yang. Tri-perspective view decomposition for geometry-aware depth completion. In *CVPR*, pages 4874–4884, 2024. 1, 5
- [46] Zhiqiang Yan, Zhengxue Wang, Kun Wang, Jun Li, and Jian Yang. Completion as enhancement: A degradation-aware selective image guided network for depth completion. *arXiv preprint arXiv:2412.19225*, 2024. 1
- [47] Lihe Yang, Bingyi Kang, Zilong Huang, Xiaogang Xu, Jiashi Feng, and Hengshuang Zhao. Depth anything: Unleashing the power of large-scale unlabeled data. In *CVPR*, pages 10371–10381, 2024. 2
- [48] Lihe Yang, Bingyi Kang, Zilong Huang, Zhen Zhao, Xiaogang Xu, Jiashi Feng, and Hengshuang Zhao. Depth anything v2. *arXiv preprint arXiv:2406.09414*, 2024. 2, 3, 4, 8, 1
- [49] Xinchen Ye, Baoli Sun, Zhihui Wang, Jingyu Yang, Rui Xu, Haojie Li, and Baopu Li. Pmbanet: Progressive multi-branch aggregation network for scene depth super-resolution. *IEEE Transactions on Image Processing*, 29:7427–7442, 2020. 2
- [50] Wei Yin, Chi Zhang, Hao Chen, Zhipeng Cai, Gang Yu, Kaixuan Wang, Xiaozhi Chen, and Chunhua Shen. Metric3d: Towards zero-shot metric 3d prediction from a single image. In *ICCV*, pages 9043–9053, 2023. 2
- [51] Jiayi Yuan, Haobo Jiang, Xiang Li, Jianjun Qian, Jun Li, and Jian Yang. Structure flow-guided network for real depth super-resolution. In *AAAI*, pages 3340–3348, 2023. 1, 2, 7
- [52] Yulun Zhang, Kungpeng Li, Kai Li, Lichen Wang, Bineng Zhong, and Yun Fu. Image super-resolution using very deep residual channel attention networks. In *ECCV*, pages 286–301, 2018. 3, 8
- [53] Zixiang Zhao, Jianshe Zhang, Shuang Xu, Zudi Lin, and Hanspeter Pfister. Discrete cosine transform network for guided depth map super-resolution. In *CVPR*, pages 5697–5707, 2022. 1, 2, 3, 5, 6, 7, 8
- [54] Zixiang Zhao, Jianshe Zhang, Xiang Gu, Chengli Tan, Shuang Xu, Yulun Zhang, Radu Timofte, and Luc Van Gool. Spherical space feature decomposition for guided depth map super-resolution. In *ICCV*, pages 12547–12558, 2023. 2, 5
- [55] Huan Zheng, Wencheng Han, and Jianbing Shen. Decoupling fine detail and global geometry for compressed depth map super-resolution. *arXiv preprint arXiv:2411.03239*, 2024. 8
- [56] Zhiwei Zhong, Xianming Liu, Junjun Jiang, Debin Zhao, and Xiangyang Ji. Deep attentional guided image filtering. *IEEE Transactions on Neural Networks and Learning Systems*, 2023. 1, 2

DuCos: Duality Constrained Depth Super-Resolution via Foundation Model

Supplementary Material

6. Metric

Given the depth prediction \mathbf{Y} and ground truth depth \mathbf{Z} , we use RMSE (cm), MAE (cm), and δ_1 accuracy for evaluation, which are defined as follows:

$$\begin{aligned} \text{MAE} &: \frac{1}{n} \sum |\mathbf{Z} - \mathbf{Y}|, \\ \text{RMSE} &: \sqrt{\frac{1}{n} \sum (\mathbf{Z} - \mathbf{Y})^2}, \\ \delta_i &: \frac{q}{n} \times 100\%, \quad q : \max(\mathbf{Z}/\mathbf{Y}, \mathbf{Y}/\mathbf{Z}) < 1.05^i. \end{aligned} \quad (18)$$

Since δ_2 and δ_3 of different DSR approaches are very close, we focus on δ_1 for comparisons.

7. Implementation Detail

Our DuCos implementation is built in PyTorch and runs on a single NVIDIA RTX 4090 GPU. The model is trained for 200 epochs using the Adam optimizer [14], with an initial learning rate of 5×10^{-5} , which is halved at epochs 40, 80, and 120. To enhance performance, we apply data augmentation techniques, including random horizontal flipping and random 90° rotation. Given that Hypersim [31] has a high resolution (1024×768), whereas the test splits of other datasets typically have much lower resolutions, we perform random 256×256 cropping when training on Hypersim. Additionally, DuCos leverages [Depth-Anything-v2-Small](#) as the default foundation model to generate prompts.

8. Complexity Analysis

Tab. 5 gives a detailed complexity comparison on the real-world RGB-D-D benchmark. Our DuCos achieves the lowest error, highlighting its superior performance. However, this comes at the expense of significant computational complexity due to the large size of the depth foundation model. Particularly, the number of trainable parameters in DuCos remains manageable at approximately 9.6 M. The primary contributor to this complexity is the large depth foundation model. Therefore, future research could explore efficient model distillation techniques to compress these large models into more lightweight counterparts while maintaining their effectiveness in prompt-based applications.

9. Scale-cross Validation

Tab. 6 presents a cross-scale performance comparison of various DSR approaches. Specifically, we evaluate models trained for $\times 4$ super-resolution directly on the more challenging $\times 8$ and $\times 16$ super-resolution tasks without

Method	Prompt	Params.	Time	Speed	RMSE
		(M)	(ms)	(FPS)	(cm)
DCTNet [53]	×	0.48	9.15	109.29	5.43
FDKN [13]	×	0.69	<u>5.78</u>	<u>173.01</u>	5.37
DKN [13]	×	1.16	17.75	56.34	5.08
FDSR [6]	×	<u>0.60</u>	5.05	198.02	5.49
SUFT [33]	×	22.01	13.33	75.19	5.41
SGNet [41]	×	8.97	33.94	29.46	5.32
SFG [51]	×	63.55	21.81	45.85	<u>3.88</u>
DA v2-S [48]	×	24.79	29.27	34.16	87.45
DuCos[†]	✓	34.38	25.09	39.86	3.68

Table 5. Complexity comparisons on the real-world RGB-D-D dataset. [†] indicates that our DuCos employs DA v2-S to produce the prompts. All methods are measured using a single 4090 GPU.

Method	scale	RGB-D-D			Lu		
		RMSE	MAE	$\delta_{1.05}$	RMSE	MAE	$\delta_{1.05}$
CUNet [5]	$\times 4 \rightarrow \times 8$	3.30	1.66	<u>97.07</u>	4.90	2.59	93.74
FDKN [13]		3.39	1.22	96.97	4.94	1.56	94.03
DKN [13]		3.31	1.22	96.97	4.86	<u>1.52</u>	<u>94.21</u>
FDSR [6]		<u>3.29</u>	<u>1.19</u>	97.01	<u>4.81</u>	1.54	94.18
DCTNet [53]		3.33	1.20	97.03	4.92	1.55	94.14
DuCos		3.19	1.17	97.11	4.64	1.46	94.28
CUNet [5]	$\times 4 \rightarrow \times 16$	5.25	2.69	92.89	7.79	3.85	87.19
FDKN [13]		5.16	2.34	92.97	7.56	2.93	87.91
DKN [13]		<u>5.15</u>	<u>2.32</u>	93.00	<u>7.54</u>	2.92	87.93
FDSR [6]		5.16	2.33	<u>93.01</u>	7.55	2.92	87.93
DCTNet [53]		<u>5.15</u>	<u>2.32</u>	92.99	7.55	2.91	88.02
DuCos		5.13	2.31	93.03	7.51	2.87	88.08

Table 6. Cross-scale DSR on the synthetic RGB-D-D and Lu.

fine-tuning. Despite this substantial scale discrepancy, our DuCos method consistently outperforms other approaches, demonstrating its superior cross-scale generalization capability. These results underscore the robustness and adaptability of DuCos in handling large-scale variations, making it a promising solution for real-world scenarios where training and testing resolutions may differ significantly.

10. Numerical Results of Arbitrary-scale DSR

Tab. 7 provides a comprehensive numerical evaluation of arbitrary-scale DSR on the synthetic datasets, corresponding to Fig. 5 in the main text. Particularly, our DuCos consistently achieves the best performance across nearly all datasets and scales, further demonstrating its robustness and effectiveness in handling the DSR task.

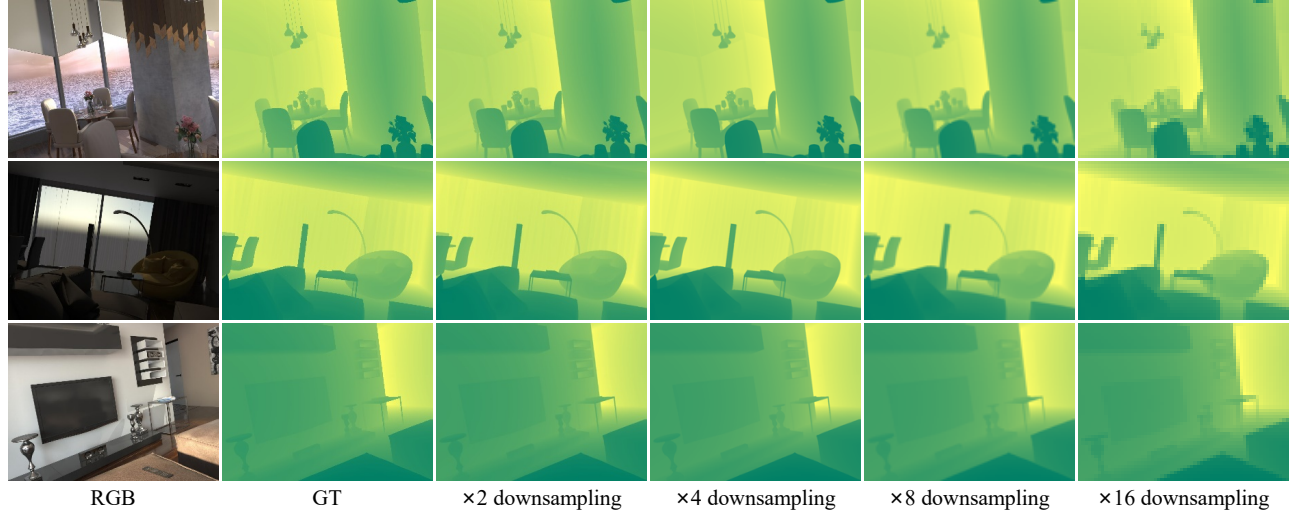


Figure 9. Visual examples of the fully synthetic Hypersim [31] dataset.

Method	Scale	Middlebury			Lu			NYU v2			RGB-D-D			TOFDSR		
		RMSE	MAE	δ_1	RMSE	MAE	δ_1	RMSE	MAE	δ_1	RMSE	MAE	δ_1	RMSE	MAE	δ_1
CUNet [5]	×1.5	<u>0.79</u>	0.46	<u>99.22</u>	<u>0.67</u>	0.30	<u>99.54</u>	1.33	0.40	99.83	0.77	0.21	99.82	2.09	0.44	99.07
FDKN [13]		1.21	0.49	98.54	1.42	0.34	99.11	1.80	0.41	99.69	0.93	0.22	99.76	1.32	0.19	99.73
DKN [13]		1.09	0.54	98.86	1.19	0.37	99.33	1.46	<u>0.35</u>	99.80	0.80	<u>0.20</u>	99.81	0.85	<u>0.13</u>	99.89
FDSR [6]		0.82	<u>0.40</u>	99.08	0.82	<u>0.28</u>	99.39	1.39	0.43	99.83	0.77	0.21	99.83	1.83	0.38	99.24
DCTNet [53]		0.89	0.48	99.12	0.91	0.32	99.45	<u>1.32</u>	0.46	<u>99.85</u>	<u>0.70</u>	0.22	<u>99.87</u>	<u>0.53</u>	<u>0.13</u>	<u>99.94</u>
DuCos		0.57	0.36	99.65	0.36	0.17	99.87	0.76	0.24	99.96	0.48	0.16	99.94	0.26	0.08	99.98
CUNet [5]	×2.7	<u>1.20</u>	0.65	98.47	<u>1.26</u>	0.50	<u>98.97</u>	2.07	0.69	99.63	<u>1.08</u>	0.32	<u>99.69</u>	2.34	0.48	99.21
FDKN [13]		1.61	0.68	98.01	1.92	0.49	98.77	2.72	0.70	99.44	1.33	0.34	99.56	2.13	0.33	99.53
DKN [13]		1.55	0.68	98.15	1.76	0.51	98.88	2.48	<u>0.65</u>	99.51	1.23	<u>0.31</u>	99.63	1.80	<u>0.26</u>	<u>99.71</u>
FDSR [6]		1.32	<u>0.62</u>	98.19	1.44	0.44	98.88	2.31	0.72	99.54	1.15	0.33	99.66	2.24	0.45	99.21
DCTNet [53]		1.30	<u>0.62</u>	<u>98.48</u>	1.34	0.42	99.04	<u>2.05</u>	0.72	<u>99.64</u>	1.07	0.32	99.71	<u>1.30</u>	0.27	<u>99.71</u>
DuCos		1.12	0.56	98.83	1.14	<u>0.43</u>	98.83	1.98	0.56	99.67	1.07	0.29	99.71	1.10	0.18	99.84
CUNet [5]	×3.4	<u>1.39</u>	0.75	<u>98.15</u>	1.47	0.60	98.75	2.69	0.91	99.42	1.32	0.43	99.54	2.85	0.67	98.87
FDKN [13]		1.74	0.75	97.80	2.07	0.54	98.62	3.15	0.85	99.32	1.50	0.40	99.46	2.60	0.42	99.39
DKN [13]		1.77	0.77	97.83	2.10	0.59	98.62	3.01	<u>0.81</u>	99.35	1.44	<u>0.38</u>	99.52	2.34	<u>0.35</u>	<u>99.55</u>
FDSR [6]		1.43	<u>0.70</u>	97.90	<u>1.46</u>	<u>0.50</u>	98.68	2.73	0.94	99.36	<u>1.30</u>	0.40	<u>99.58</u>	3.01	0.69	98.64
DCTNet [53]		1.55	0.71	98.01	1.69	0.53	<u>98.78</u>	<u>2.58</u>	0.93	<u>99.48</u>	1.32	0.42	<u>99.57</u>	<u>1.92</u>	0.44	99.44
DuCos		1.33	0.62	98.52	1.35	0.40	99.16	2.37	0.70	99.55	1.19	0.33	99.64	1.69	0.26	99.71
CUNet [5]	×5.3	1.93	0.91	97.36	1.82	0.68	<u>98.33</u>	3.69	1.25	99.07	1.69	0.53	99.27	3.60	0.83	98.51
FDKN [13]		2.08	0.91	97.17	2.35	<u>0.66</u>	98.20	4.07	1.23	99.04	1.88	0.53	99.18	3.50	0.63	98.96
DKN [13]		1.96	<u>0.88</u>	<u>97.47</u>	2.28	<u>0.66</u>	98.25	<u>3.62</u>	1.10	99.20	1.76	<u>0.50</u>	<u>99.29</u>	3.40	0.60	99.03
FDSR [6]		<u>1.92</u>	0.91	97.33	2.19	0.69	98.18	3.66	<u>1.13</u>	<u>99.17</u>	1.75	0.51	99.25	3.18	<u>0.61</u>	98.96
DCTNet [53]		2.06	0.91	97.08	2.27	0.67	97.96	3.72	1.31	<u>99.05</u>	1.90	0.58	99.11	<u>3.27</u>	0.72	98.58
DuCos		1.88	0.81	97.68	<u>2.15</u>	0.56	98.48	3.60	1.17	99.20	<u>1.73</u>	0.49	99.30	3.42	0.63	<u>99.01</u>
CUNet [5]	×11.6	3.65	1.73	92.72	4.14	1.47	94.79	6.70	2.72	97.08	2.94	1.09	97.93	5.82	1.76	96.11
FDKN [13]		3.25	1.50	94.28	3.86	1.25	95.36	6.04	2.36	97.74	2.85	1.00	<u>98.14</u>	5.66	1.52	96.76
DKN [13]		3.20	1.46	94.60	3.96	1.27	95.20	5.91	2.29	97.87	2.89	0.99	98.09	5.85	<u>1.51</u>	<u>96.89</u>
FDSR [6]		<u>3.14</u>	<u>1.43</u>	<u>94.62</u>	<u>3.72</u>	<u>1.19</u>	<u>95.61</u>	6.01	<u>2.24</u>	<u>97.92</u>	<u>2.85</u>	<u>0.96</u>	98.11	5.82	<u>1.51</u>	96.81
DCTNet [53]		3.88	1.82	91.86	4.68	1.57	93.58	7.14	3.09	96.33	3.45	1.25	97.48	5.95	1.61	96.35
DuCos		2.84	1.22	95.99	3.66	1.01	96.56	<u>5.99</u>	2.11	98.13	2.84	0.90	98.25	<u>5.79</u>	1.29	97.49

Table 7. Quantitative comparisons with arbitrary scaling factors on the synthetic DSR benchmark datasets.

11. More Visualizations

Fig. 9 presents some RGB-D examples from the fully synthetic Hypersim [31] dataset, demonstrating its high-quality and realistic scenes. Fig. 11 shows visual comparisons at $\times 2$, $\times 4$, $\times 8$, and $\times 16$ scales on the synthetic NYU v2,

while Fig. 12 illustrates results for arbitrary-scale DSR. Additionally, Fig. 10 showcases visual results on the real-world RGB-D-D and TOFDSR benchmark datasets. These visualizations further confirm that our DuCos effectively enhances depth predictions, yielding more precise shapes, sharper edges, and improved structural consistency.

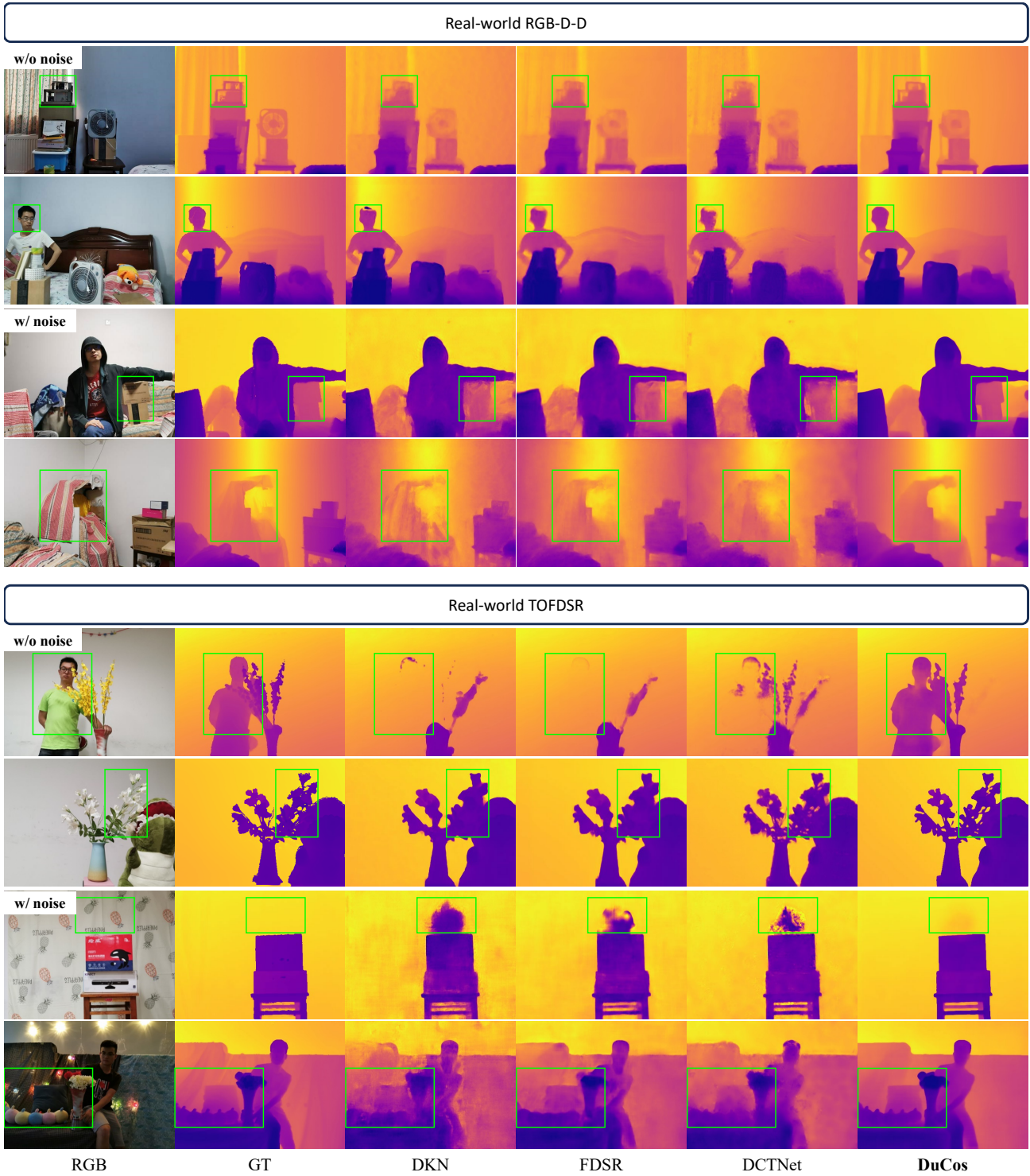


Figure 10. Visual comparisons of different DSR methods with and without noise on the real-world RGB-D-D and TOFDSR datasets.

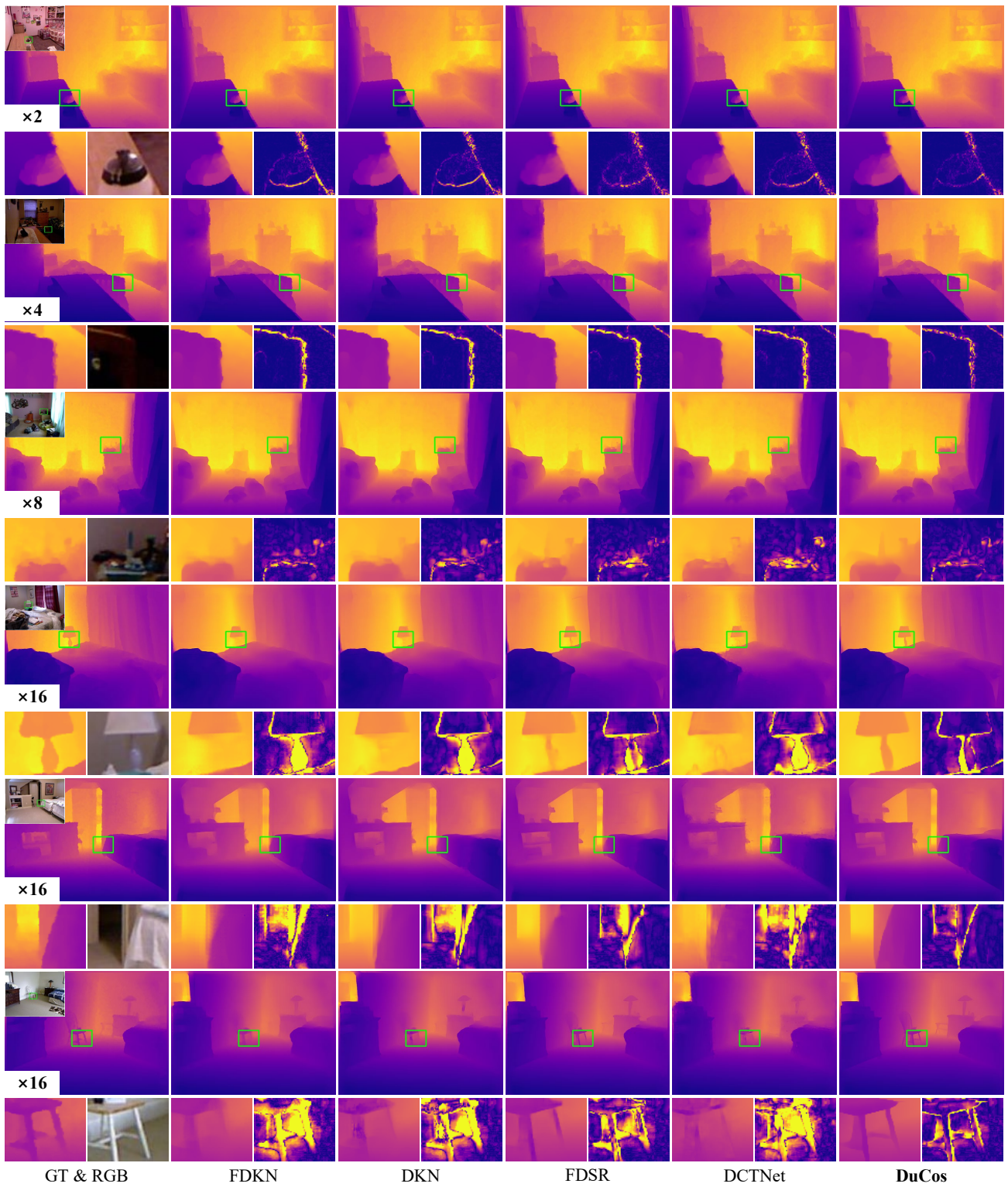


Figure 11. Visual comparisons of different DSR methods with $\times 2$, $\times 4$, $\times 8$, and $\times 16$ scaling factors on the synthetic NYU v2 dataset.

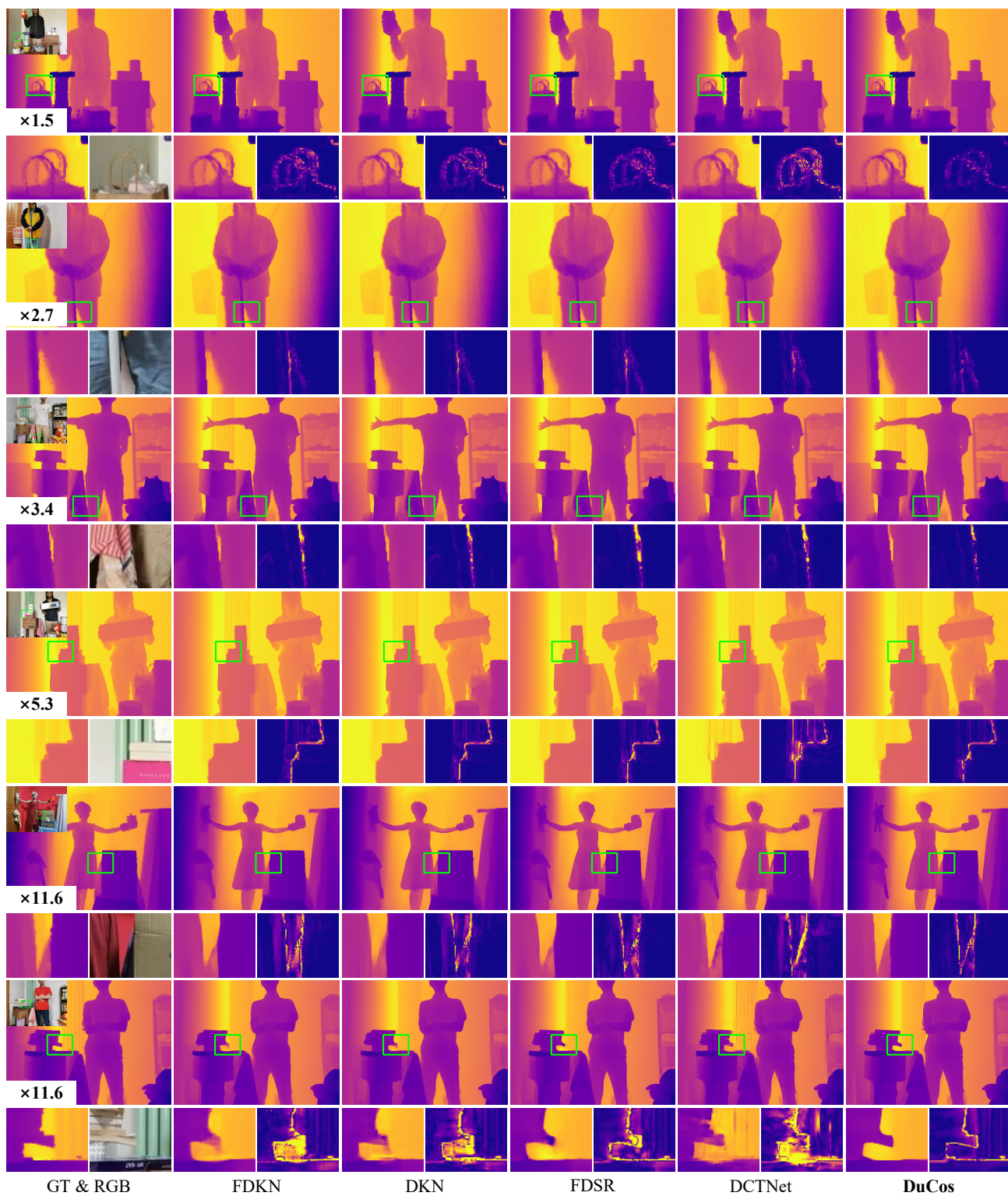


Figure 12. Visual comparisons of different methods with $\times 1.5$, $\times 2.7$, $\times 3.4$, $\times 5.3$, and $\times 11.6$ scales on the synthetic RGB-D-D dataset.